Supporting Information

Experimental Demonstration of Localized Plasmonic Structured Illumination Microscopy

Joseph L. Ponsetto[1], Anna Bezryadina[1], Feifei Wei[2], Keisuke Onishi[3], Hao Shen[1], Eric Huang[2], Lorenzo Ferrari[4], Qian Ma[1], Yimin Zou[3] and Zhaowei Liu[1]*

[1]Department of Electrical and Computer Engineering, University of California, San Diego, 9500 Gilman Drive, La Jolla, California 92093, USA

[2]Department of Physics, University of California, San Diego, 9500 Gilman Drive, La Jolla, California 92093, USA

[3]Department of Biology, University of California, San Diego, 9500 Gilman Drive, La Jolla, California 92093, USA

[4]Materials Science and Engineering, University of California, San Diego, 9500 Gilman Drive, La Jolla, California 92093, USA

***e-mail: zhaowei@ucsd.edu**

Contents:

1. Super-resolution image reconstruction

Because the LP field excitation patterns in the LPSIM method were generated on nano-antennas rather than via a standing wave, the structured illumination profile was not a simple shifted sine wave, as is the case for many SIM experiments. Although the LPSIM substrate was carefully designed and simulated to ensure it would provide the appropriate patterns for super-resolution, it is difficult to expect perfect knowledge of the real patterns at the 60 nm scale, due to fabrication tolerances and other sources of experimental error. To reconstruct a super-resolution image using the more complex, quasi-periodic patterns and pattern shifts present in LPSIM, a variant of blind-SIM[27] was used. This reconstruction method is very useful as it does not require perfect knowledge of the real excitation patterns. Suppose an unknown fluorescent-tagged object o is excited by nine LP field patterns $I_{l=1,\ldots,9}$. For each pattern, the image m recorded by the camera is the convolution of the excited object and the PSF,

$$m_l(\boldsymbol{r}) = \int o(\boldsymbol{r}')\, I_l(\boldsymbol{r}')\, h(\boldsymbol{r}-\boldsymbol{r}')\, d\boldsymbol{r}' \tag{S1}$$

where $\boldsymbol{r}$ is the position in the object plane, and h is the PSF. In this "blind" scheme, both the object o and the excitation patterns I_l are treated as unknowns. So, we have 9 equations and ten unknowns. To make this system of equations solvable, an additional constraint will be introduced.

If it is assumed that over the nine sub-images, the total excitation is approximately equal throughout the object plane, then we can write

$$I_9 = 9\bar{I} - \sum_{l=1}^{8} I_l \tag{S2}$$

where $\bar{I}$ is the average excitation intensity. An iterative error-minimization algorithm is used to steadily improve initial estimates for the 9 unknown 2D matrices, o and $I_{1,\ldots,8}$.

The residual error R_l is defined as the difference between the measured images m_l and the images we would expect to measure based on the PSF and the current estimates for the object and excitation pattern. Thus we can define a cost function

$$F\ \left(o,\{I_l\}\right) = \sum_{l=1}^{9} \|R_l\|^2 = \sum_{l=1}^{8} \left\|m_l - (I_l \cdot o) * h\right\|^2 + \left\|m_9 - (I_9 \cdot o) * h\right\|^2 \tag{S3}$$

where $*$ represents convolution. Iteratively improved estimates for o_n and $I_{l,n}$ (where n represents the iteration count) are found using the conjugate gradient method. Since the object intensity can never be negative, a positivity constraint was incorporated into the cost function, improving reconstruction stability with respect to experimental noise. The camera pixels, with magnification, had 67 nm effective size. To improve the smoothness of the final reconstruction, the measured images were interpolated prior to reconstruction. Occasional experimental drift was also corrected using reference point orientation for each sub-image, when necessary.

Shown below in Fig. S1 are three example diffraction-limited sub-images collected during experiment.

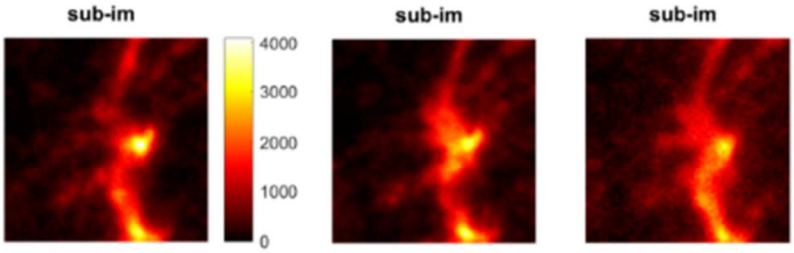

Figure S1 | LPSIM sub-images: Raw images collected for different laser angles incident to the LPSIM substrate with a neuron sample. Scale bar is EMCCD count (linear). As different areas of the object are excited on a sub-wavelength scale, the diffraction-limited image changes significantly. Note that other experimental factors may also contribute to the changes in an unpredictable fashion, making the blind algorithm doubly important.

2. Fabrication details

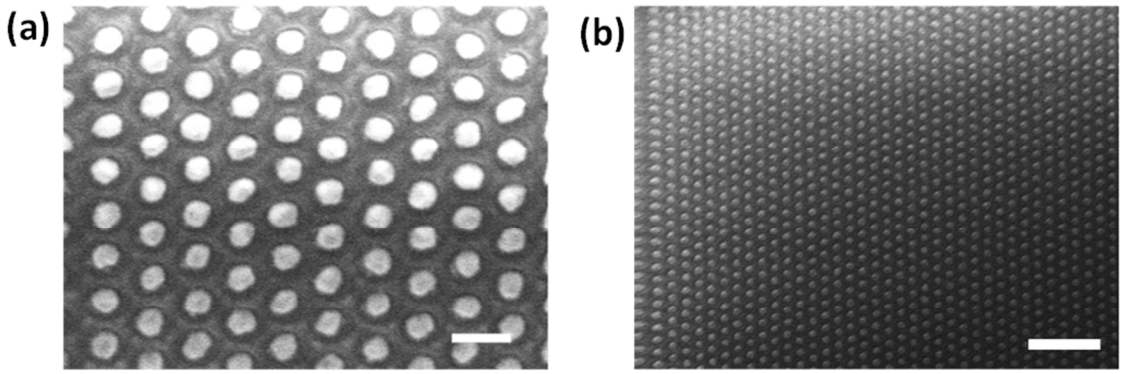

Figure S2 | (a),(b) SEM images of nanodisc array from above, showing silver discs arranged in a hexagonal lattice. Shown here is the larger-featured array, with disc diameter of 80 nm and pitch of 200 nm. Scale bars represent 200 nm and 1 μm, respectively.

The nano-antenna geometry was designed via full-wave simulation to provide a 3x resolution enhancement using LPSIM. This scheme is scalable to different wavelengths, as long as a good plasmonic material is chosen. For this reason, two versions of the LPSIM substrate were made, at different scales. Each patterned covered a 2 mm^2 area, to allow for a very wide super-resolved field of view. Both arrays consisted of a hexagonal lattice of nanodiscs embedded in fused silica.

In the smaller-scaled array, the discs were 60 nm in diameter, 60 nm in height, and spaced 150 nm apart from the nearest neighbor, measured center-to-center. This smaller array was designed to use silver as the metallic element, and works best with laser wavelengths in

the short end of the visible spectrum, such as 405 nm or 488 nm. All of our experimental images shown in this work were taken using the smaller-featured array. The larger-featured pattern (shown in Fig. S2) had 80 nm diameter discs, still 60 nm in height, spaced 200 nm from their nearest neighbors. This array was designed to use gold as the metallic element, and works best with laser wavelengths in the middle or longer end of the visible spectrum, such as 532 nm. This design can be useful if a particular biological sample is very sensitive to shorter-wavelength light, although the resolution performance will be somewhat less.

One significant advantage of generating structured excitation via local geometry is that the pattern will be less prone to distortion. Whereas in SIM or PSIM, an interference-based standing wave depends on a reliable and undisturbed phase relationship between counter-propagating waves in the object plane, LPSIM does not. If there is a local defect in the substrate, or if the object itself perturbs the intended field pattern, the defect will not cause the pattern to deteriorate outside of the localized area.

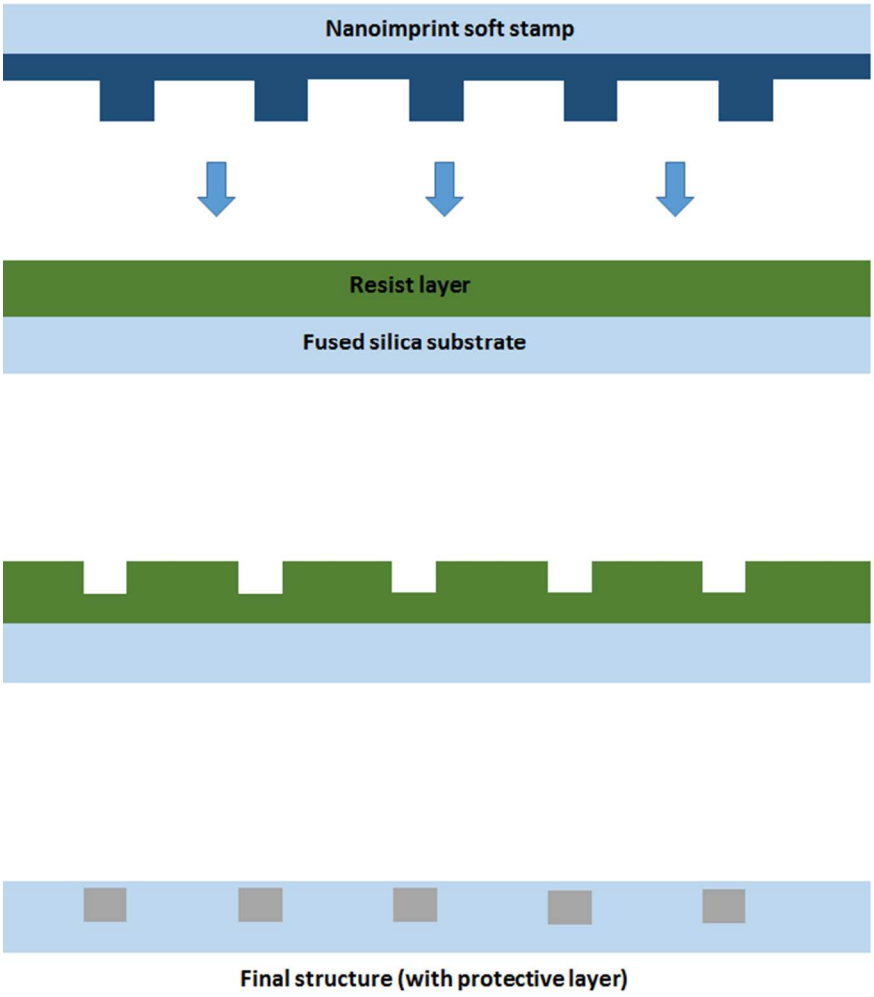

Figure S3 | Cross-sectional outline of fabrication steps: Top, nanoimprint stamp is impressed onto resist. Middle, result of nanoimprint process. Bottom, finished nano-antenna array after etching and deposition.

Shown in Fig. S3 is a summary of the fabrication process. Nanoimprinting was used to allow for inexpensive, repeatable results. Our three-step etching process was calibrated by cross-sectional scanning electron microscope (SEM) images, as in Fig. 3d, which allowed for accurate adjustment of our etch times.

This structure was designed according to careful full-wave simulations and subsequent analytical imaging calculations. Shown in Fig. S4 are the full-wave simulations of the LPSIM excitation patterns in the object plane for three different incident laser angles. The results are analogous for the other two symmetry axes, giving a total of nine distinct illumination patterns for use in experiment. Note that the patterns are not uniformly translated, and are not perfectly sparse in spatial frequency. Despite this, both in simulation and experiment, super resolution reconstruction is achieved. The important characteristics of useable LPSIM excitation pattern sets are (1) that the intensity varies significantly from pattern to pattern everywhere in the field of view, and (2) the primary spatial frequencies of the pattern give the desired Moiré effect to enable collection of sub-diffraction information with a far-field imaging setup.

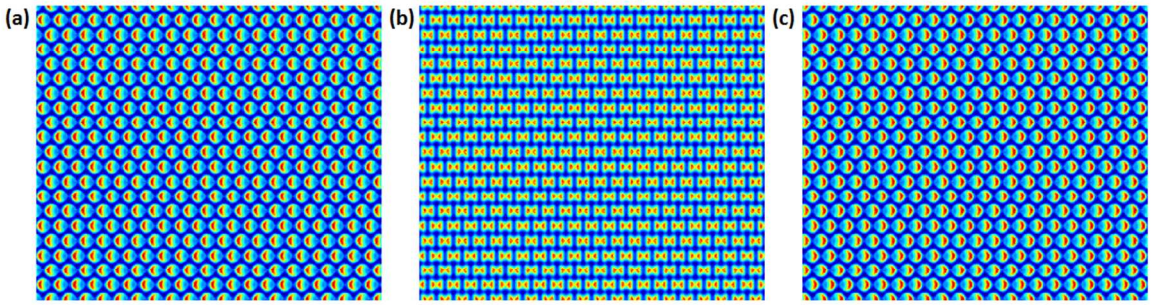

Figure S4 | Simulated excitation patterns: Plasmonic intensity distribution (linear scale) in the object plane created by laser light incident to the LPSIM substrate at angles of (a) 60°, (b) 0°, and (c) -60° relative to the normal, along one of the three symmetry axes traced in Fig. 3(b).

The fabrication result always has some variability and error relative to the theoretical design. This generally results in a rounding of the disc geometry, and roughness of the disc surface. As long as these imperfections are fairly uniform and minor, the consequences for performance will be fairly small. Samples were tested for quality using SEM, FIB, and simple spectrum measurements to confirm geometry and uniformity of plasmonic response. If the sample had major differences from the design, there could be significant issues such as strong nearest neighbor coupling of the LP fields (if the discs are too large) or incomplete object plane coverage (if the discs are too small). The resonant wavelength will also be affected by major changes in the geometry. This can actually be used to the advantage of the designer; if operation at a second wavelength is desired, the array can be made with an intentionally larger or smaller set of geometrical parameters, as long as one stays within the plasmonically active wavelength range of the antenna material.

3. Experimental details

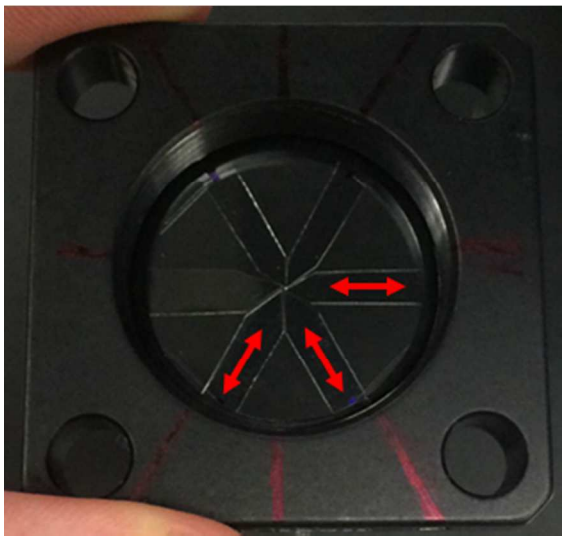

Figure S5 | Custom polarizer plate: Strips of wire grid polarizing film were cut and placed as shown, with the allowed polarization direction indicated by the red arrows, along the length of the strips. This enabled us to passively maintain in-plane polarization while rapidly changing the incident laser angle within our 4f system.

To ensure the proper polarization was used at all times during our 2D laser angle scan, a custom polarizer plate was designed (Fig. S5). Edmund Optics wire grid polarizer film was used due to a good compromise between power damage threshold, extinction ratio, and the practicality of cutting custom shapes out of the polarizer material. The polarizer was placed between the two lenses of our 4f system, where beam position corresponds to incident angle in the object plane. Exactly normal incident laser light was not used, as the beam was distorted by the polarizer edges at this angle. This polarization selection method inevitably causes insertion loss, but its passivity has the advantages of both simplicity and instantaneous response. As an initial proof-of-concept experiment focusing on super-resolution performance, the imaging speed of the LPSIM technique was not pushed to its maximum in this paper. Based on already-demonstrated 11 Hz SIM imaging[16], combined with a resonant LP field enhancement factor in the object plane which we have both predicted and observed to be more than 5x, we are confident that future work will demonstrate fast, video-rate imaging capability.

A Measurement Computing 1208HS digital acquisition (DAQ) device was used with a MATLAB script to automate the LPSIM experiment. A preset sequence of nine voltages was sent to each of the mirrors to control incident angle, while a synchronized trigger signal initiated the

camera exposures. The captured image data was loaded into MATLAB for super-resolution reconstruction. A cylindrical lens in front of our 4f system corrected for a practical path-length issue. Our two scanning mirrors were separated 5 mm apart along the optical path. Thus, only one could be at the optimal position for our 4f system. The cylindrical lens left the correctly-placed mirror angle unaltered, but adjusted the effective angle of the out-of-position mirror to give the desired 2D angle sequences.